



OPEN Acoustic emission characteristics and damage constitutive model of fractured sandstone under uniaxial compression

Qiang Liu^{1,2,5}, Chao Pan^{2✉}, Lin Yan², Xuguang Wang¹, Shujian Li³ & Juncai Cao⁴

To investigate the statistical laws of acoustic emission energy (AEE) avalanche dynamics of sandstone under varying fracture lengths and dip angles, as well as to determine the relationship between acoustic emission (AE) parameters and damage variables, we studied the mechanical properties and AE characteristics of sandstone with a single fracture subjected to uniaxial compression with the aid of the Shimadzu AG-IS test system and the PCI-2 AE system. The AEE characteristics of fractured sandstone under load were analyzed based on the statistical method of avalanche dynamics, with emphasis on AEE distribution, aftershock sequence, and waiting time distribution. The Weibull distribution function that incorporates a correction coefficient β was employed to optimize the Weibull parameters based on the strain equivalent hypothesis theory, which led to the establishment of a statistical damage constitutive model for fractured rock. The results indicated that the peak strength of rock samples initially decreases and then increases with increasing fracture dip angle, and decreases with increasing fracture length. The AEE of the rock sample followed a power-law distribution, with a power-law index ranging from 1.62 to 1.81, which was independent of fracture length and dip angle. The aftershock sequence also adhered to a power-law distribution, whereas the waiting time exhibited a multi-power-law distribution. The proposed statistical damage constitutive model aligned more closely with the experimental curves compared to previous models that normalizes AEE.

Keywords Fractured rock mass, Acoustic emission experiment, Damage constitutive model, Avalanche dynamics

Fractured sandstone is a prevalent rock mass in underground mining, which is characterized by a variety of fracture morphologies that contribute to complex mechanical properties and weakening of the rock mass. This condition can lead to instability and failure of rock strata, resulting in engineering disasters such as roof caving and pillar instability. Therefore, it is of great engineering significance to study the mechanical properties and damage evolution of fractured sandstone to ensure the safety of underground mining operations. In addition, the examination of the acoustic emission (AE) characteristics of fractured sandstone can provide a scientific basis and technical support for the monitoring and prediction of underground mining^{1–4}.

For fractured rock samples, Yang et al.⁵ conducted uniaxial compression tests on red sandstone containing a single non-straight fracture with the aid of the AE monitoring system. They found that the peak strength of rock samples increased approximately linearly with increasing fracture dip angle, and the AE counts of fractured rock samples were more dispersed than those of intact rock samples. Wang et al.⁶ observed that prefabricated fractures were prone to shear microcracks during the failure process of rock samples as the dip angle increased. Wang et al.⁷ performed uniaxial compression tests on low-strength rock samples with various geometric fractures and revealed that the influence of prefabricated fractures with different geometric characteristics on rock samples varies significantly. The failure modes of rock samples were controlled by fracture dip angle, and the impacts of the fracture number and vertical fractures on rock failure were much greater than that of horizontal fractures. Niu et al.⁸ concluded that fractures reduce the load-bearing capacity of red sandstone, and that the AE parameter b value can serve as a prediction index for large-scale fractures. Guo et al.⁹ utilized AE parameters to explore the mechanism of granite microcracks, where three stages of initial calm, slow AE development, and fast AE

¹Southwest Jiaotong University, Chengdu 430070, China. ²Guizhou University Mining College, Guiyang 550025, China. ³Yunnan Phosphate Chemical Group Co., Ltd., Kunming 650600, Yunnan, China. ⁴Guizhou Energy Group Co., Ltd., Guiyang 550081, Guizhou, China. ⁵POLY EXPLOSIVE HAMI CO., LTD, Hami 939000, China. ✉email: cpan@gzu.edu.cn

development were clarified. Moradian et al.¹⁰ established a correlation between acoustic emission energy (AEE) and the size of crack events by integrating rock stress-strain diagrams with AE parameters. Chen et al.¹¹ analyzed the relationship between the crack closure effect and the aspect ratio through conducting uniaxial compression tests on sandstone samples, and then established a nonlinear energy dissipation model based on the crack closure effect. Peng et al.¹² defined the energy storage coefficient and energy dissipation coefficient, and then performed loading tests on sandstone samples with different dip angles. Their findings indicated that the larger the rock fracture dip angle, the stronger the energy storage capacity and the weaker the energy dissipation capacity. The macroscopic fragmentation deformation of rock can be interpreted as the accumulation of numerous small ‘avalanche’ events¹³, which can be captured by an AE monitoring system. Previous studies have employed avalanche dynamics theory to analyze the AE parameters related to rock fragmentation^{14–16}.

Regarding the damage constitutive model of fractured rock mass, Xia et al.¹⁷ established a damage constitutive model for fractured sandstone by coupling the initial damage caused by microscopic defects and the macroscopic cracks in rock samples. Also, a compaction coefficient was introduced to modify the model. Miao et al.¹⁸ established a damage constitutive model for fractured rock based on Weibull distribution and Drucker-Prager criterion. They also deduced the hydrochemical physical damage from porosity. Wang et al.¹⁹ examined the damage evolution of rock samples with different pore sizes and utilized AE ring counts to optimize Weibull parameters for constructing a damage constitutive model. Lv et al.²⁰ established a total damage model based on Lemaitre strain equivalence hypothesis under the coupling of macroscopic and mesoscopic damage. Li et al.²¹ conducted laboratory triaxial compression tests on sandstone to determine the distribution coefficient and void damage influence coefficient, and then constructed a statistical rock void damage model. While the aforementioned research provides valuable reference and theoretical support for constructing the damage constitutive models for fractured rock samples, studies regarding the establishment of a damage constitutive model based on AEE for fractured rock samples with different geometric shapes remain relatively rare.

Based on the insights from previous studies, the present study investigated the AE signal characteristics and energy evolution during the deformation and failure processes of fractured sandstone with the aid of laboratory uniaxial compression tests and AE monitoring system. This study also analyzed the variations in mechanical parameters, AE signal, and energy under different fracture dip angles and lengths. The AE parameters were statistically analyzed through avalanche dynamics, and the distributions of AEE, aftershock sequence, and waiting time across different fracture configurations were examined. The AE cumulative energy was employed to elucidate the damage state of fractured sandstone, and a correction coefficient β was proposed to construct a damage constitutive model suitable for fractured rock. The research findings are expected to hold significant engineering value for predicting strength of fractured rock mass in practical applications.

Experimental equipment and scheme

The sandstone samples used in this study were sourced from Chongqing, China. The sandstone blocks were processed into standard samples with a diameter of 50 mm and a height of 100 mm. The prefabricated fractures, which measure 1 mm in width, were introduced into rock samples, among which the fractures with a length of 15 mm were equipped with dip angles of 0°, 15°, 30°, 45°, 60°, 75°, and 90°, respectively, while those with lengths of 20 mm and 25 mm were only equipped with a dip angle of 60°.

For the uniaxial compression tests, each rock sample was subjected to testing using a Shimadzu AG-IS material testing machine at a strain rate of 0.01 mm/min, while the AE signals were captured using the PCI-2 AE monitoring system. Prior to testing, two AE sensors were strategically placed on opposite sides of the lower part of the sample, and secured with transparent rubber rings. To ensure accurate results, an appropriate amount of coupling agent (vaseline) was applied between the AE sensor and the sample surface, with a threshold set to 40 dB. The uniaxial compression test system, AE monitoring system, and strain acquisition system were subsequently activated to gather the requisite data for analysis, as depicted in Fig. 1.

Test results

Stress–strain curve of rock sample

Figure 2 illustrates the stress–strain curves for sandstone samples with different fracture dip angles, while Fig. 3 presents the stress–strain curves for sandstone samples with different fracture lengths. Analyses of the data revealed that the stress–strain curves for rock samples with various geometric fractures display similar trends, which can be divided into distinct stages: the pore compaction stage, the nearly linear elastic deformation stage, as well as the plastic deformation and failure stage.

As illustrated in Fig. 2, the peak strength of rock samples initially decreased and then increased with increasing fracture dip angle. The peak strength of rock sample with a fracture length of 15 mm and a fracture dip angle of 0° was 48.43 MPa. Compared with the peak strength of rock sample with a fracture dip angle of 0°, the peak strength was reduced by 12.65 MPa for rock sample with a fracture dip angle of 15°, while those were increased by 3.02 MPa, 13.08 MPa, 21.50 MPa, 33.62 MPa, and 39.10 MPa for rock samples with fracture dip angles of 15°, 30°, 45°, 60°, 75°, and 90°, respectively, with a decrease rate of 26.12% and increase rates of 6.23%, 27%, 44.39%, 69.42%, and 80.73%, respectively.

Figure 3 demonstrated that the peak strength of rock samples decreases gradually.

With increasing fracture length. The peak strength of rock sample with a fracture length of 10 mm and a fracture dip angle of 60° was 93.92 MPa. Compared with the peak strength of rock sample with a fracture length of 10 mm, the peak strength of rock samples with fracture lengths of 15 mm, 20 mm, and 25 mm were reduced by 23.98 MPa, 27.99 MPa, and 34.74 MPa, respectively, with reduction rates of 25.53%, 29.80%, and 40.18%, respectively.

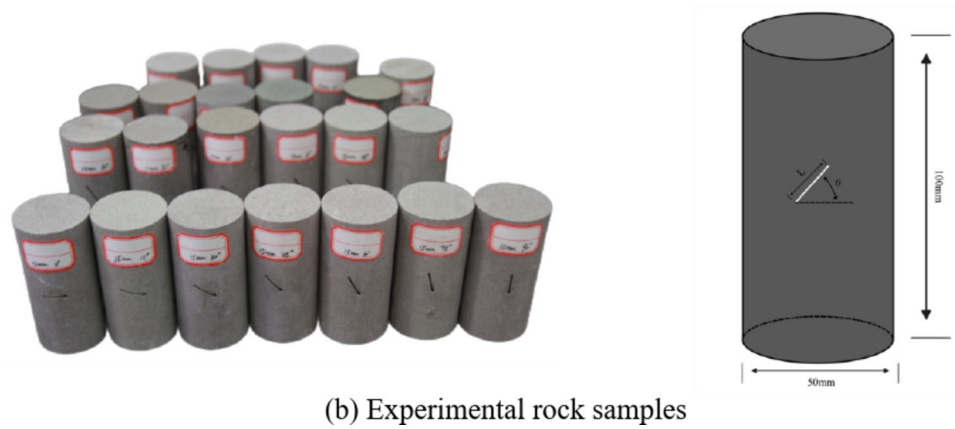
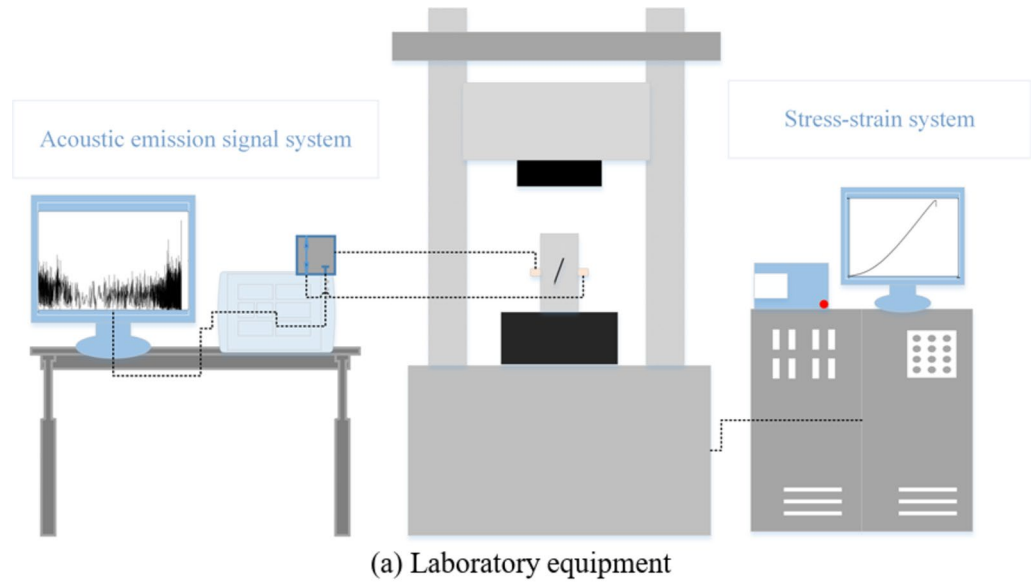


Fig. 1. Experimental equipment and samples.

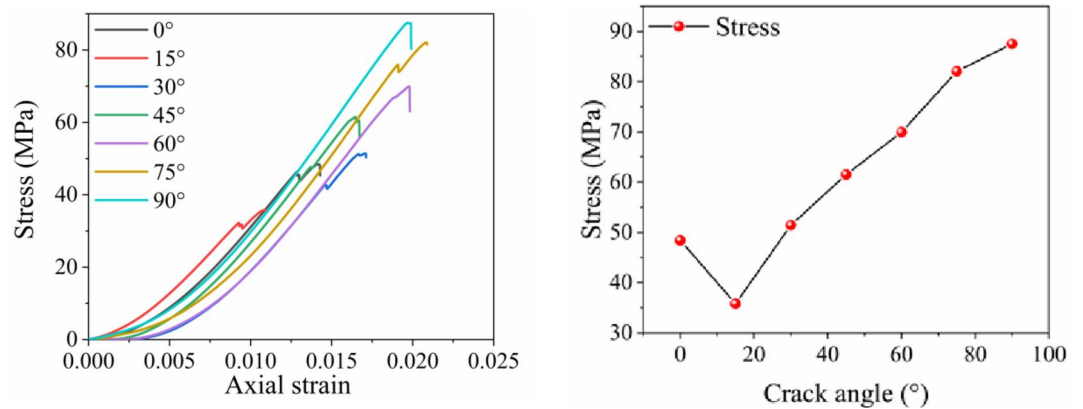


Fig. 2. Stress–strain curves with different inclination angles.

The peak strength of rock samples was significantly affected by the geometric parameters of prefabricated fractures. As the fracture dip angle increased, the peak strength of rock samples initially declined and then increased linearly. Analyses revealed that when the fracture direction was parallel to the loading direction, the applied load was maximized. Additionally, the peak strength of rock samples greatly decreased significantly as the fracture length increased. As the fracture length increased, the internal damage to the rock sample intensified, ultimately diminishing its load-bearing capacity.

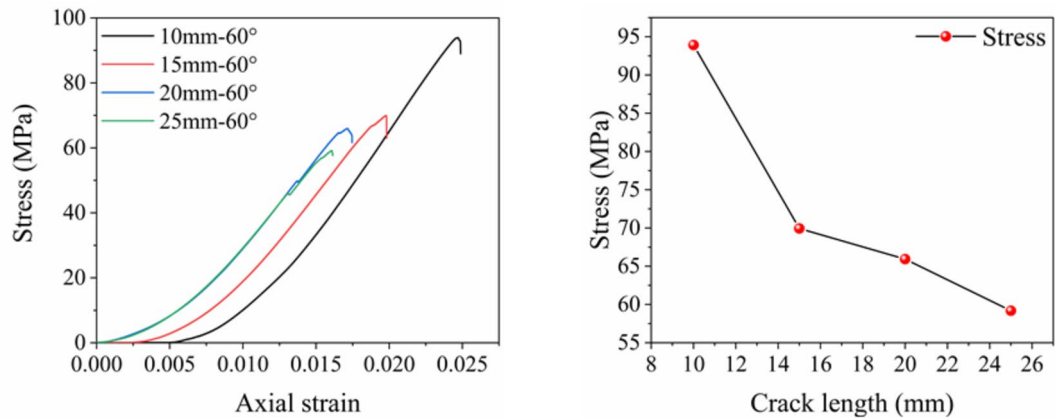


Fig. 3. Stress–strain curves of different crack lengths.

AE characteristics of rock samples with different geometric fractures

In rock mechanics tests, AE can effectively monitor the real-time failure processes of rock samples. The characteristics of AE parameters aligned closely with the failure processes of rock samples. Changes in AE characteristics can be categorized into four stages: the pore compaction stage, the elastic deformation stage, the plastic deformation stage, and the failure stage.

- During the initial loading stage, the presence of microvoids and prefabricated geometric fractures within the rock sample led to pore compaction and fissure development. This stage was characterized by a rapid strain increase, with the experimental curve exhibiting a concave shape. The occurrence of micro-fractures was frequent, resulting in dense and frequent AE events.
- As the load on the rock sample gradually increased, the defects and micropores were compressed, and the sample entered the elastic deformation stage. During this stage, the experimental curve exhibited an approximately linear shape. Micro-fracture events were relatively infrequent, and AE events were monitored less frequently. Although the distribution of AE events was sparse, their frequency gradually increased as the load continued to rise.
- As the load continued to increase, the yield strength of the rock sample was gradually approached, and the sample entered the plastic deformation stage. During this stage, microcracks expanded and developed into macroscopic cracks, which propagated and deformed under the influence of the external load. The number of cracks gradually increased, resulting in a dense distribution of AE events.
- During this stage, the rock sample reached its peak strength, resulting in the formation of a fracture surface. The internal structure of the rock sample was destroyed, leading to block sliding. At this stage, there was a significant increase in AE events, with a higher density of occurrences, resulting in a peak AEE value.

The number of AE events served as a valuable indicator for characterizing the internal fracture evolution process of rocks, as depicted in Fig. 4. The AEE value also effectively expressed the degree of rock failure, and this relationship remained unaffected by the prefabricated geometric fracture morphology. The AE parameters were instrumental in characterizing the damage levels of rock samples. To further investigate the AE characteristics of rock samples with prefabricated fractures, this study employed the avalanche dynamics for statistical analysis.

AE-based statistical law of avalanche dynamics of fractured sandstone failure AEE probability density distribution

Figure 5 displays the probability density distribution of AE with respect to the AEE interval during uniaxial compression failure of rock samples with varying geometric fractures, which was obtained through the histogram method. The vertical axis represents the AEE probability density, while the horizontal axis represents the AEE interval. This method involves pre-dividing the AEE interval beforehand and then selecting a group distance to calculate the probability density. The probability density distribution of AEE for fractured samples with varying dip angles was presented using a double logarithmic coordinate system.

Selecting the interval from 10^1 – 10^5 allowed for fitting the probability density. A strong linear relationship between $P(Q)$ and Q in the logarithmic coordinates was observed. The results indicated that the AEE distribution throughout the compression failure process of the sample follows a power-law distribution, which adhered to the Gutenberg-Richter law ($P(Q) \sim Q^{-F}$) to a certain extent:

$$P(Q)dQ \sim Q_{1-F}^{-F}/Q_{\min}^{1-F}dQ, Q > Q_{\min} \quad (1)$$

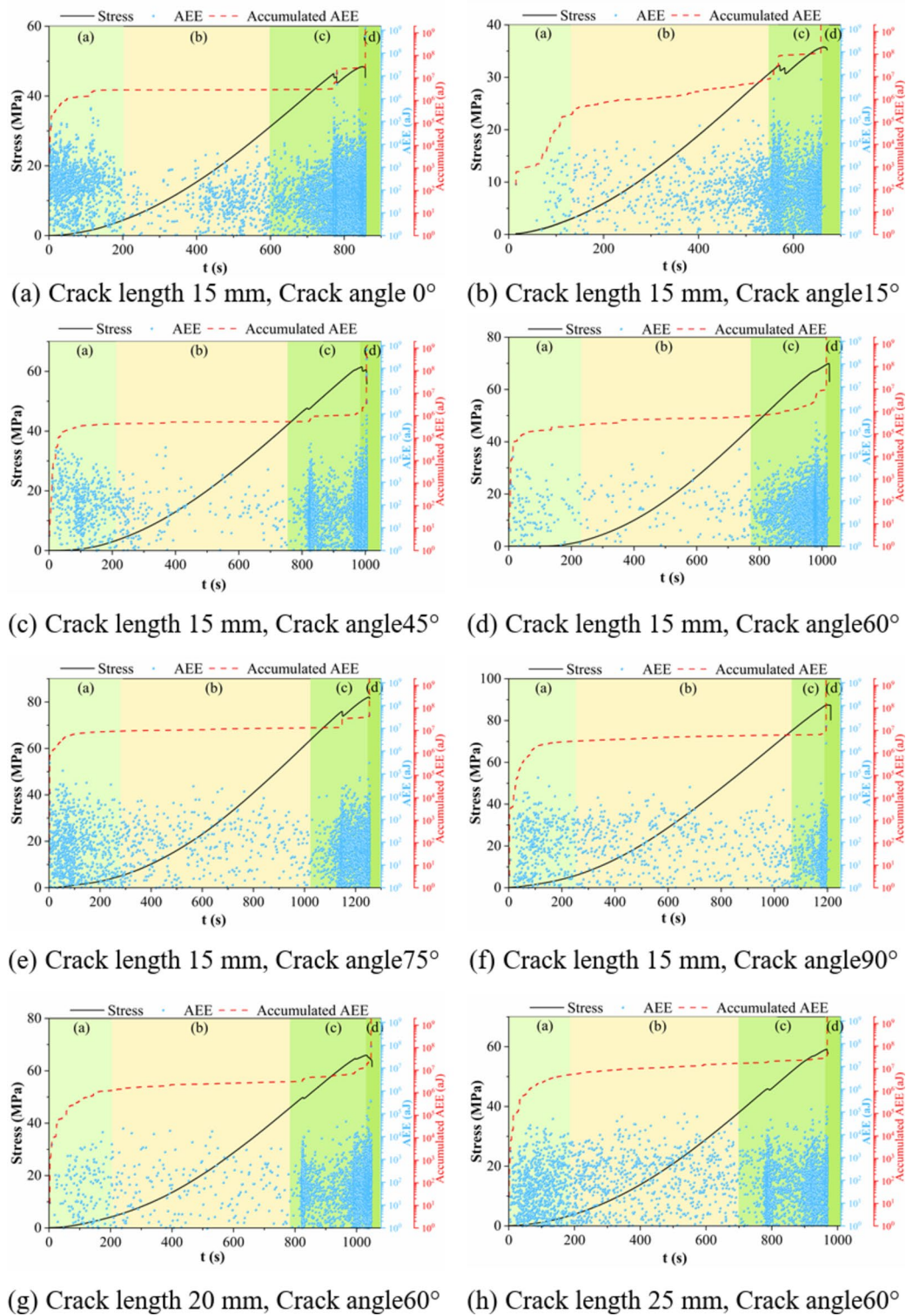


Fig. 4. Acoustic emission curves of rock samples with different defects.

where Q_{min} is the normalized parameter, Q is the AEE, F is the AEE power-law index, and $P(Q)$ is the AEE probability density function.

As shown in Fig. 5, the AEE followed a power-law distribution and was not affected by prefabricated geometric fractures. With an increase in fracture dip angle, the power-law index exhibited a slight increase, which was generally around 1.7. As the fracture length increased, the power-law index demonstrated a slight downward trend. The decrease may be attributed to the fact that longer prefabricated fracture in rock sample

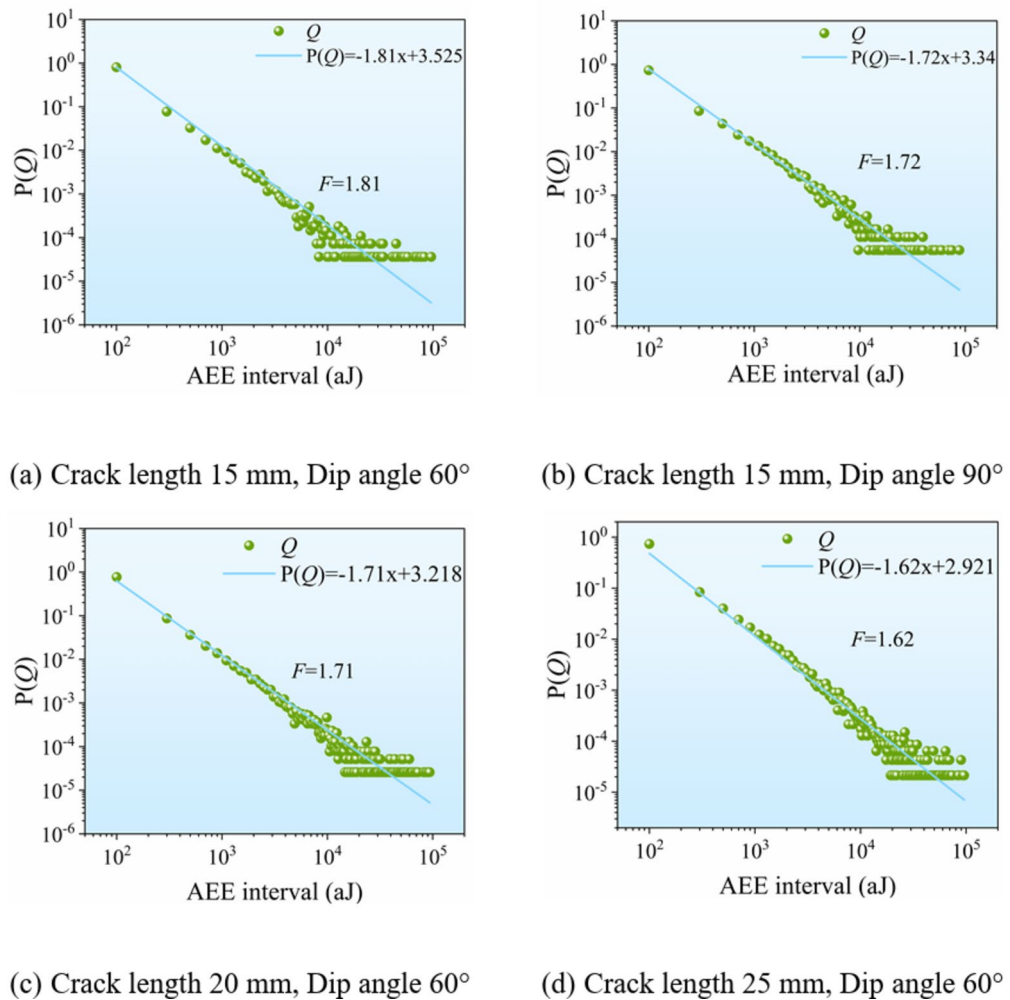


Fig. 5. AEE probability distribution diagram of rock samples with different geometric defects.

resulted in a higher degree of internal damage, which facilitated the formation and expansion of new cracks, thereby generating in a large number of AE events. The overall power-law index fell between 1.62 and 1.81.

Aftershock sequence distribution

In the analysis of seismic monitoring data, the strongest energy was defined as the main shock, while the others after the main shock were named as aftershocks. The distribution of the aftershock sequence was described using the Omori-Uzaki law, which characterized the attenuation of aftershock frequency over time. AE data with AEE values ranging from 10^1 to 10^4 were artificially selected as the main shock, while the remaining data were designated as the aftershock sequence until the next main shock energy. Three energy intervals, i.e., 10^1 – 10^2 , 10^2 – 10^3 , 10^3 – 10^4 , were delineated, and the aftershock frequency (N as s^{-1}) in each interval was calculated against the time difference ($t-t_{ms}$).

Figure 6 illustrates the distribution of aftershock sequences across different energy intervals plotted on a double logarithmic coordinate axis. For rock sample with a fracture length of 15 mm and a fracture dip angle of 60° , the aftershock sequences in different energy intervals exhibited a robust linear relationship, with the power law index approximating 1.1.

Waiting time distribution

The time difference between AE events was defined as the waiting time, which is expressed as $t = t_{i+1} - t_i$, where t_{i+1} and t_i are the monitoring times of adjacent AE signals.

Figure 7 displays the distribution of waiting time during the compression failure process of the rock sample with a fracture length of 15 mm and a fracture dip angle of 60° , where P_Q is the probability density function of the waiting time distribution, δ is the waiting time difference, (n) is the average number of AE events per unit time.

According to Fig. 7, the data demonstrated a strong linear relationship under the double logarithmic coordinate axis, which indicated that the waiting time distribution conforms to the power-law distribution and

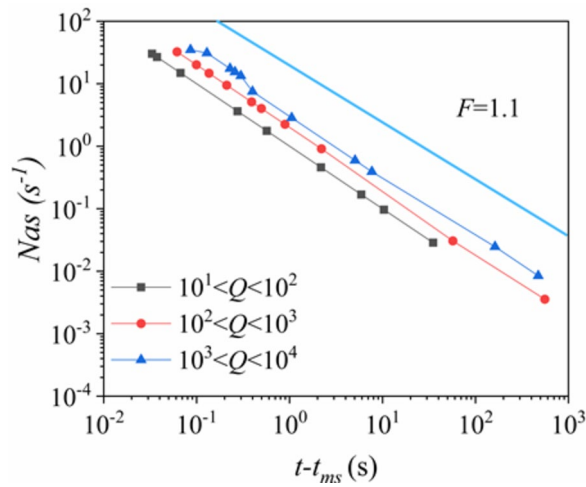


Fig. 6. Distributions of Omori-Utsu’s law in different acoustic emission energy subsets of the rock sample with a fracture length of 15 mm and a dip angle of 60°.

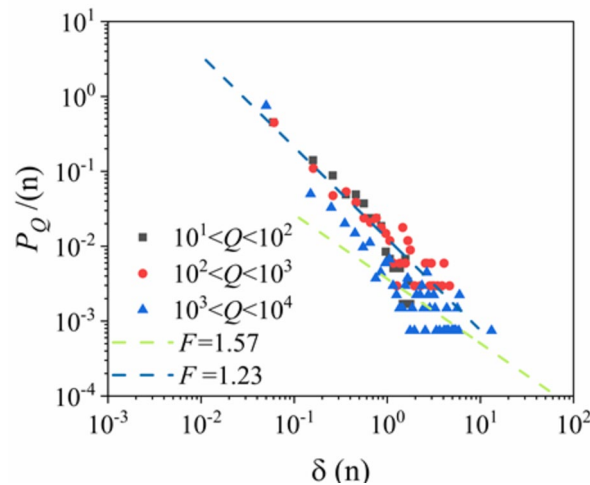


Fig. 7. Distribution of waiting time for the rock sample with a fracture length of 15 mm and a fracture dip angle of 60°.

exhibits a multi-power law distribution feature. The power-law exponent of the waiting time distribution in the 0.1 s to 1 s interval was approximately 1.23, while that in the 1 s to 100 s interval was about 1.57.

Damage constitutive model for fractured sandstone

Statistical damage constitutive model

Lemaitre²² established the following damage constitutive model based on the strain equivalence hypothesis proposed in the context of material damage process.

$$\sigma = E\varepsilon \cdot (1 - D) \tag{2}$$

where σ is the effective stress, D is the damage variable, E is the material deformation modulus, and ε is the strain.

Given the complexity of internal micro-element damage for rock samples subjected to the external load, numerous scholars have referenced the Weibull distribution to analyze the micro-element change behavior of the rock under load^{23,24}. The probability density function for the rock micro-unit is expressed as follows.

$$f(\varepsilon) = \lambda\gamma(\lambda\varepsilon)^{\gamma-1} \exp(-(\lambda\varepsilon)^\gamma) \tag{3}$$

where ε is the deformation, λ is the shape parameter, γ is the scale parameter.

Kachanov²⁵ defined the damage variable D using the micro-defect area formed by damage relative to the initial apparent area of the material as follows.

$$D = \frac{A_d}{A} \tag{4}$$

where A_d is the fracture area of the sample during compression, and A approximately considers the fracture area when there is no damage before loading.

$$A_d = \int_0^\varepsilon Af(x)dx = A \{1 - \exp(-(\lambda\varepsilon)^\gamma)\} \tag{5}$$

Combining Eqs. (4) and (5) yields:

$$D = 1 - \exp(-(\lambda\varepsilon)^\gamma) \tag{6}$$

Combining Eqs. (2) and (6) yields:

$$\sigma = E\varepsilon \cdot \exp(-(\lambda\varepsilon)^\gamma) \tag{7}$$

where the Weibull distribution parameters λ and γ can be determined by the peak stress-strain point:

$$\frac{\partial\sigma}{\partial\varepsilon} |(\varepsilon_s, \sigma_s) = 0 \tag{8}$$

where σ_s is the peak stress, and ε_s is the strain corresponding to the peak stress.

$$\gamma = \frac{1}{\ln\left(\frac{E\varepsilon_s}{\sigma_s}\right)}, \lambda = \frac{1}{\varepsilon_s} \left(\frac{1}{\gamma}\right)^{\frac{1}{\gamma}} \tag{9}$$

Damage constitutive model based on AEE

AE monitoring can capture the energy released by rock micro-fractures²⁶. According to the cumulative AEE of rock samples, the degree of damage can be quantified. The damage variable D_q can be expressed as follows.

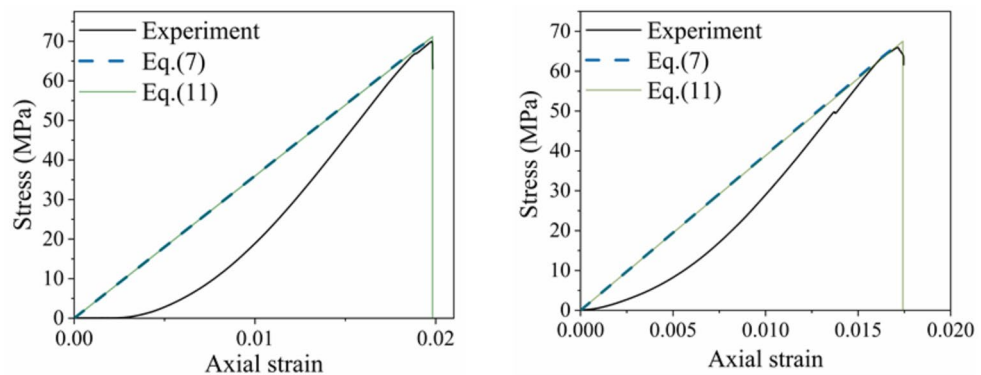
$$D_q = \frac{Q_f}{Q_z} \tag{10}$$

where Q_f is the cumulative AEE at any time, Q_z is the AEE accumulated in the AE peak energy value stage. Combing Eqs. (2) and (10) yields:

$$\sigma = E\varepsilon \cdot \left(1 - \frac{Q_f}{Q_z}\right) \tag{11}$$

As indicated in Fig. 8, the damage model based on AEE aligned well with traditional damage constitutive model.

Equation (11) featured a linear decline stage of stress, which was attributed to the fact that the cumulative energy value was very close to the maximum cumulative energy value. Both models exhibited substantial errors relative to the experimental results.



(a) Crack length 15 mm, Dip angle 60° (b) Crack length 20 mm, Dip angle 60°

Fig. 8. Damage constitutive model constructed by Eqs. (7) and (11).

Damage constitutive model for coupling analysis of AEE and Weibull distribution

To control the error range between the results obtained from the model and the experimental values, many scholars have utilized AEE and AE ringing counts to optimize the Weibull function^{27,28}. In this study, AEE was employed to optimize the Weibull distribution parameters, and a correction coefficient β was proposed to minimize the discrepancies between Eqs. (7), (11), and the experimental values.

Combining Eqs. (6) and (10) yields:

$$D_q = 1 - \exp(-(\lambda\varepsilon)^\gamma) \quad (12)$$

The damage amount obtained by AEE was fitted to the Weibull coefficient, which allowed for the derivation of the damage constitutive model.

$$\sigma = E\varepsilon \cdot \exp(-(\lambda_q\varepsilon)^{\gamma_q}) \quad (13)$$

At the onset of the experiment, a compaction process occurred within the sample. To accurately characterize this process, the correction coefficient β was proposed as follows.

$$\beta = \varepsilon \cdot \lambda_q \quad (14)$$

where λ_q is the Weibull shape parameter of AEE fitting, and ε is the strain. The specific values of λ_q obtained through the conducted test are presented in Table 1. The complete AE-based cumulative energy damage constitutive model can be obtained by combining Eqs. (13) and (14).

Figure 9 presents the damage constitutive model constructed from Eqs. (7) and (15). Equation (15) demonstrated greater consistency with the test curve compared to Eqs. (7) and (11). Thus, it well characterized the concave curve shape caused by micro-cracks and pore compaction during the initial experimental stage. The damage constitutive model that incorporates AE cumulative energy could better reflect the stress-strain curve of sandstone with different geometric fractures during uniaxial compression.

Discussion and analysis

Based on the results and analyses presented, the AE parameter characteristics released during the rock failure process can be divided into three stages according to the AE density, as depicted in Fig. 10.

In the first stage, the number of AE events was large, but the energy value was generally low. This phenomenon was due to the fact that the presence of pre-existing micro-voids and artificial prefabricated fractures within the rock sample resulted. In the second stage, the rock sample entered the elastic stage, during which AE events were less frequently monitored, the stress and strain increased linearly, and the concave curve from the previous stage transitioned a straight line. In the third stage, due to the accumulation of damage within the rock mass, the degree of damage was significantly elevated to reach the damage limit of rock sample. Internal micro-cracks gradually expanded, followed by block sliding, ultimately leading to the failure of the rock sample. In this stage, the number of AE events was extremely large, while both the energy value and stress reached their peaks simultaneously.

Regarding the statistical analysis results of avalanche dynamics, the AEE power-law index obtained in this study ranged from 1.62 to 1.81. Given that the probability density of AEE was artificially selected. For precise determination of the value range of the power law exponent F , maximum likelihood estimation was utilized to mitigate the associated uncertainty. The maximum likelihood estimation was employed to diminish this error, and its calculation formula is presented as follows.

$$F = 1 + n \left[\sum_{i=1}^n \ln(Q_i/Q_{\min}) \right]^{-1} \quad (16)$$

where F is a power-law index, Q_{\min} is the lower limit of normalization, Q_i is the monitored AEE, which satisfies $Q_i > Q_{\min}$.

The standard deviation expression is estimated as follows.

$$e = \left(\frac{F(Q_{\min}) - 1}{\sqrt{n}} \right) + o\left(\frac{1}{n}\right). \quad (17)$$

The AEE data in Fig. 5(a) was statistically analyzed using the maximum likelihood method. The calculation results are depicted in Fig. 11, where the red solid line represents the power-law index F obtained by the maximum likelihood method, the green area represents the standard deviation, and the black dotted line represents the power-law index F obtained by the histogram method. As illustrated in Fig. 11, the power-law index selected

Fracture length-fracture dip angle	15 mm and 60°	15 mm and 75°	20 mm and 60°	25 mm and 60°
λ_q	50.46	47.89	57.4	62

Table 1. Weibull distribution parameters.

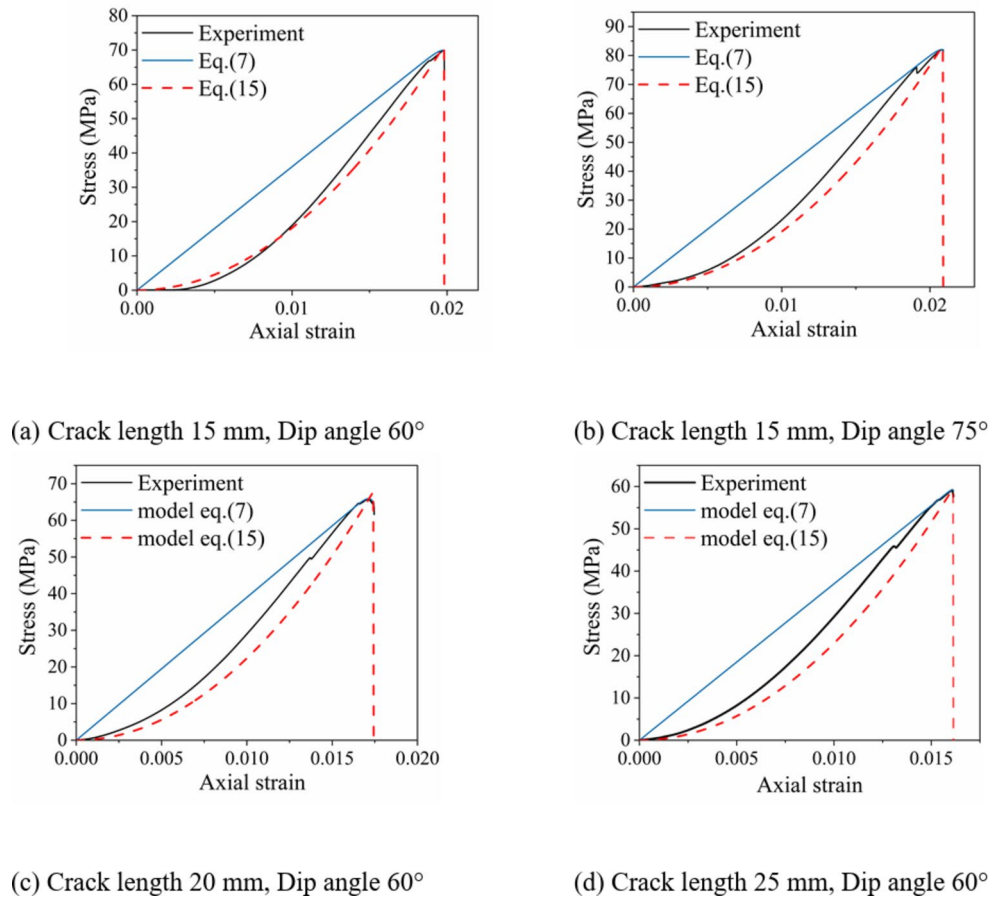


Fig. 9. Damage constitutive model constructed by Eqs. (7) and (15).

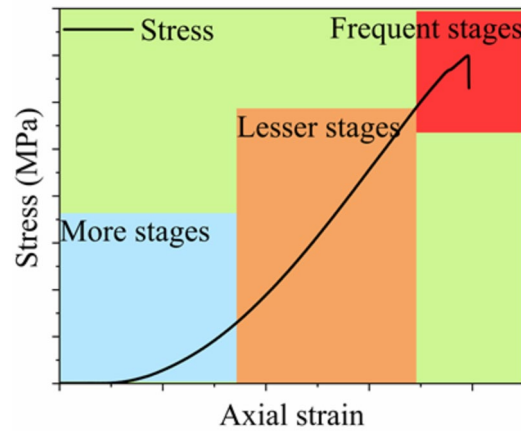


Fig. 10. AE parameter characteristics.

via the histogram method was lower than the initial shoulder gap of the maximum likelihood method, thereby validating the reliability of the power law index obtained through the histogram method.

In this study, a damage constitutive equation that considers AEE was established, and the correction coefficient β was proposed to improve the model. This model demonstrated a good agreement with the experimental values. The correction parameter was calculated based on the Weibull shape parameter λ_q and strain ε , where $1/\lambda_q$ is the statistical average strain value.

Figure 12 illustrates the correction coefficients for rock samples with a fracture dip angle of 60° and fracture lengths of 15 mm, 20 mm, and 25 mm. The λ_q increased with increasing fracture length, which may be attributed

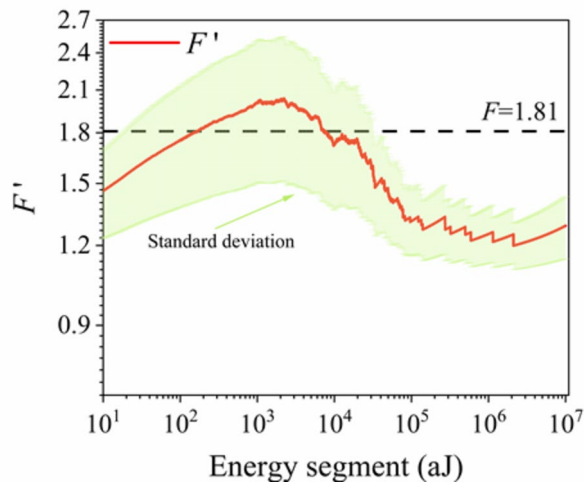


Fig. 11. Maximum likelihood estimation of AEE power-law index.

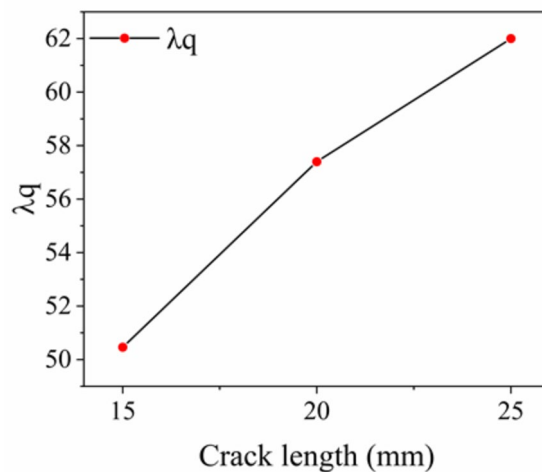


Fig. 12. Correction coefficient β value.

to the fact that longer prefabricated fracture lead to greater damage to the rock mass, consequently reducing its load-bearing capacity.

To explore the microstructure of rock samples with different geometric fractures after uniaxial compression failure, the fracture surfaces of rock samples with a fracture dip angle of 60° and fracture lengths of 15 mm, 20 mm and 25 mm were tested using SEM, and then the SEM images were obtained. Existing research indicated that the macroscopic fracture behaviors of rocks are closely related to their microscopic defects. The common fracture modes in rocks include transgranular and intergranular fractures, which often exhibit distinctive patterns, such as step pattern, river pattern, and tongue pattern^{29,30}.

In Fig. 13(a), (b), and (c), numerous microcracks and macrocracks were observed. Figure 13(a) depicted a typical fracture morphology. Figure 13(b) presented a relatively flat fracture surface characterized by a river pattern and a high fracture density. Figure 13(c) showed secondary cracks oriented perpendicular to the axial stress, along with some micro-cracks and macro-cracks. Figure 13(d), (e), and (f) lacked consistent fracture characteristics. Figure 13(d) displayed clear texture with a few massive rock masses resembling step patterns. Figure 13(e) illustrated an uneven fracture surface, with no obvious macroscopic defects, while the tongue pattern was distinctly observable. Figure 13(f) revealed large macroscopic cracks and a step pattern similar to the stepped morphology. The analyses indicated that the prefabrication of different geometric fractures can alter the microscopic characteristics of the fracture surface of rock samples following mechanical loading.

Conclusions

This study investigated the mechanical properties and AE evolution characteristics of fractured rock with different geometric fractures. Subsequently, a damage constitutive model was developed for fractured sandstone. The main conclusions are as follows.

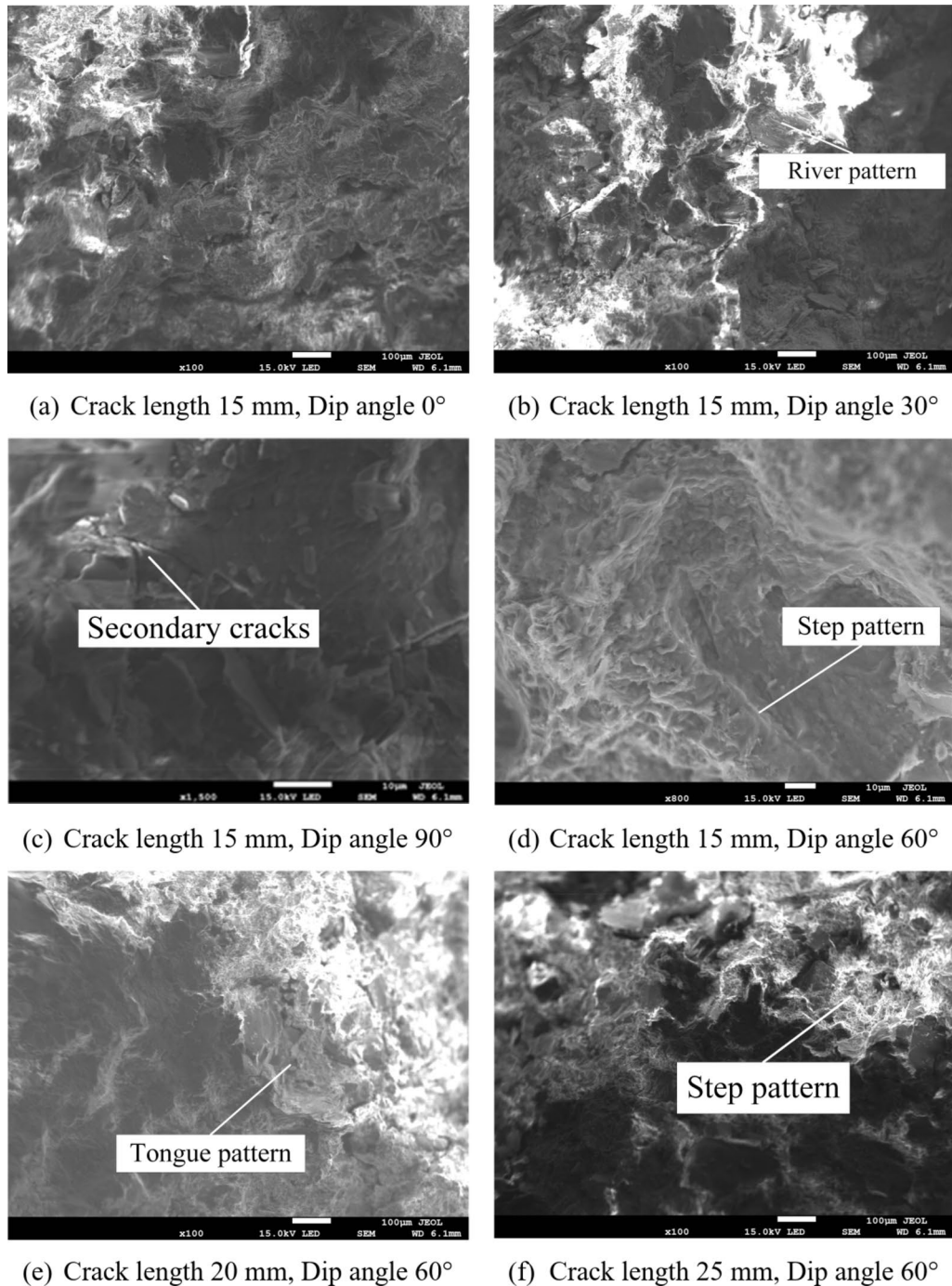


Fig. 13. Scanning electron microscope image.

- (1) The stress-strain curves of rock samples were influenced by the dip angle and length of the fracture. The peak strengths of rock samples with a fracture length of 15 mm and fracture dip angles of 0° , 15° , 30° , 45° , 60° , 75° and 90° were analyzed. Except for the peak strength of the 15° rock sample, which was 12.65 MPa lower than that of the 0° rock sample, the remaining samples exhibited approximate linear growth. The peak strength of rock samples with a fracture dip angle of 60° and fracture lengths of 10 mm, 15 mm, 20 mm, and 25 mm were discussed, where the peak strength decreased approximately linearly with increasing fracture length.
- (2) AE parameters effectively characterized the stress trend. Throughout the mechanical loading process, the rock samples transitioned sequentially through the pore compaction stage, elastic deformation stage, plastic deformation stage, and failure stage. The AE signal density and energy value accurately represented these four stages.

- (3) The AEE distribution of rock samples with different geometric fractures demonstrated a robust power-law distribution. The power-law index of AEE distribution was minimally impacted by the fracture dip angle. As the fracture length increased from 15 mm to 20 mm and 25 mm, the power-law index decreased from 1.81 to 1.71 and 1.62, respectively, with reduction rates of 5.6% and 10.5%. The waiting time distribution and the aftershock sequence conformed to the power-law distribution, while the waiting time distribution followed a multi-power-law distribution.
- (4) A damage variable was constructed based on the cumulative energy of AE. The damage constitutive correction coefficient β was determined by λ_g and the experimental strain value according to the Weibull distribution principle. Compared with the damage equation and statistical damage constitutive constructed by normalizing AEE, the proposed model aligned more closely with the experimental curve.

Data availability

Because some data of this paper will be used in the next research plan of the research group, the data sets generated and/or analyzed in this study are not public, but are available from the corresponding author on reasonable request.

Received: 22 October 2024; Accepted: 1 January 2025

Published online: 24 January 2025

References

1. Xu, Y. et al. Mechanical characteristics and damage evolution law of sandstone with prefabricated cracks under cyclic loading. *Arab. J. Sci. Eng.* **46**, 10641–10653 (2021).
2. Min, D. et al. Acoustic emission characteristics and damage law for prefabricated single-crack sandstone under uniaxial compression. *Struct. Control Health Monit.* **29** (10), 3018 (2022).
3. Li, X. W. et al. Mechanical properties and energy evolution of fractured sandstone under cyclic loading. *Materials* **15** (17), 6116 (2022).
4. Du, Y. T. et al. Experimental study of mechanical and permeability behaviors during the failure of sandstone containing two preexisting fissures under triaxial compression. *Rock Mech. Rock Eng.* **53**, 3673–3697 (2020).
5. Yang, S. Q. et al. Experiment and peridynamic simulation on cracking behavior of red sandstone containing a single non-straight fissure under uniaxial compression. *Theoret. Appl. Fract. Mech.* **108**, 8442 (2020).
6. Wang, Y. Q. et al. Experimental and numerical simulation study of crack coalescence modes and microcrack propagation law of fissured sandstone under uniaxial compression. *Theoret. Appl. Fract. Mech.* **115**, 8442 (2021).
7. Wang, Y. et al. Experimental study on mechanical properties and failure modes of low-strength rock samples containing different fissures under uniaxial compression. *Eng. Fract. Mech.* **197**, 1–2 (2018).
8. Niu, Y., Zhou, X. & Zhou, L. Fracture damage prediction in fissured red sandstone under uniaxial compression: acoustic emission b-value analysis. *Fatigue Fract. Eng. Mater. Struct.* **43**, 175–190 (2019).
9. Guo, T. Y. & Wong, L. N. Y. Microcracking behavior of three granites under mode I loading: insights from acoustic emission. *Eng. Geol.* **278**, 7952 (2020).
10. Moradian, Z., Einstein, H. H. & Ballivy, G. Detection of cracking levels in brittle rocks by parametric analysis of the acoustic emission signals. *Rock Mech. Rock Eng.* **49**, 785–800 (2016).
11. Chen, Y. & Guo, B. Crack closure effect and energy dissipation model for rocks under uniaxial compression. *Geotech. Geol. Eng.* **38**, 621–629 (2019).
12. Peng, K. et al. Effect of crack angles on energy characteristics of sandstones under a complex stress path. *Eng. Fract. Mech.* **218**, 7944 (2019).
13. Salje, E. K. H. et al. Noise of collapsing minerals: predictability of the compressional failure in goethite mines. *Am. Mineral.* **98**, 609–615 (2013).
14. Pan, C. et al. Mechanism and control technology of strong ground pressure behaviour induced by high-position hard roofs in extra-thick coal seam mining. *Int. J. Min. Sci. Technol.* **32**, 499–511 (2022).
15. Jiang, X. et al. Predicting mining collapse: Superjerks and the appearance of record-breaking events in coal as collapse precursors. *Phys. Rev. E* **96**, 004 (2017).
16. Nataf, G. F. et al. Predicting failure: acoustic emission of berlinite under compression. *J. Phys. Condens. Matter* **26**, 27540 (2014).
17. Xia, B. W. et al. Effect of crack angle on mechanical behaviors and damage evolution characteristics of sandstone under uniaxial compression. *Rock Mech. Rock Eng.* **55**, 6567–6582 (2022).
18. Miao, S. et al. Damage constitutive model and variables of cracked rock in a hydro-chemical environment. *Arab. J. Geosci.* **11**, 19 (2018).
19. Wang, J. J. et al. Experimental investigation of damage evolution and failure criterion on hollow cylindrical rock samples with different bore diameters. *Eng. Fract. Mech.* **260**, 7944 (2022).
20. Lv, S. Q. et al. Study on macro-meso damage model of sandstone with open cracks under freeze-thaw load coupling. *Rock Mech. Eng.* **42**, 1000–6915 (2023).
21. Li, Y. M. et al. Study on statistical damage model of rock considering void effect. *Coal Sci. Technol.* **50**, 120–125 (2022).
22. Lemaitre, J. How to use damage mechanics. *Nucl. Eng. Des.* **80**, 233–245 (1984).
23. Li, Y. Q. et al. Energy evolution and damage constitutive model of anchored jointed rock masses under static and fatigue loads. *Int. J. Fatigue* **167**, 0142–1123 (2023).
24. Chen, S. et al. Comparative study on three-dimensional statistical damage constitutive modified model of rock based on power function and Weibull distribution. *Environ. Earth Sci.* **77**, 108 (2018).
25. Kachanov, L. M. Time of the rupture process under creep conditions. *Izv Akad. Nank S S R Otd Tech. Nauk.* **8**, 1 (1958).
26. Gu, Q. et al. Acoustic emission characteristics and damage model of cement mortar under uniaxial compression. *Constr. Build. Mater.* **213**, 377–385 (2019).
27. Zheng, Q. et al. Failure mechanism of different types of shotcrete based on modified Weibull distribution model. *Constr. Build. Mater.* **224**, 306–316 (2019).
28. Behnia, A. et al. Damage detection of SFRC concrete beams subjected to pure torsion by integrating acoustic emission and Weibull damage function. *Struct. Control Health Monit.* **23**, 51–68 (2015).
29. Xie, H. & Chen, Z. D. Microscopic mechanism analysis of rock fracture. *J. China Coal Soc.* **02**, 57–67 (1989).
30. Zuo, J. P. et al. Fractography of sandstone failure under temperature-tensile stress coupling effects. *Chin. J. Rock Mech. Eng.* **191** (12), 2444–2457 (2007).

Acknowledgements

This work was supported by the Youth fund project of the national natural science foundation of China (52204129, 52464012, 52164016, 52164006), the Science and technology supporting project of Guizhou Province (Qian Ke He Zhi Cheng[2023]General 273,248), the Guizhou Provincial Fund Project (Grant Nos. (2022) ZD001), the Scientific Research Project of Introducing Talents in Guizhou University (No. 202045), the Guizhou Geological Exploration Fund Project (52000024P0048BH101732), Tianchi Young Doctor Program in Xinjiang Uygur Autonomous Region (XJTCYC2022(1)-BLMB1), Tianchi Talents Leading Talents Program Project in Xinjiang Uygur Autonomous Region (XJTCYC2023(2)-BLMB1, XJTCYC2023(2)-BLMB2).

Author contributions

Qiang Liu: Conceptualization, Writing—original draft, Data curation. Chao Pan: Methodology, Writing—Review. Xuguang Wang: Supervision. Lin Yan: Investigation. Shujian Li: software. Juncai Cao: Visualization.

Declarations

Competing interests

The authors declare no competing interests.

Additional information

Correspondence and requests for materials should be addressed to C.P.

Reprints and permissions information is available at www.nature.com/reprints.

Publisher's note Springer Nature remains neutral with regard to jurisdictional claims in published maps and institutional affiliations.

Open Access This article is licensed under a Creative Commons Attribution-NonCommercial-NoDerivatives 4.0 International License, which permits any non-commercial use, sharing, distribution and reproduction in any medium or format, as long as you give appropriate credit to the original author(s) and the source, provide a link to the Creative Commons licence, and indicate if you modified the licensed material. You do not have permission under this licence to share adapted material derived from this article or parts of it. The images or other third party material in this article are included in the article's Creative Commons licence, unless indicated otherwise in a credit line to the material. If material is not included in the article's Creative Commons licence and your intended use is not permitted by statutory regulation or exceeds the permitted use, you will need to obtain permission directly from the copyright holder. To view a copy of this licence, visit <http://creativecommons.org/licenses/by-nc-nd/4.0/>.

© The Author(s) 2025